Simultaneous waveform inversion of SWD data for P-wave velocity, density, and source parameters

Jinji Li, Scott Keating, Kris Innanen, and Roman Shor

ABSTRACT

Full-waveform inversion (FWI), an optimization-based approach to estimating subsurface models, is limited by incomplete acquisition and illumination of the subsurface. Adding data corresponding to new and independent ray paths as input could significantly increase FWI models' reliability. In principle, seismic-while-drilling (SWD) technology can supply these additional ray paths; however, it introduces a new suite of unknowns, namely precise source locations (i.e., drilling path), source signature, and radiation characteristics. Here we formulate a new FWI algorithm in which source radiation patterns and positions join the velocity and density values of the grid cells as unknowns to be determined. We then conduct several numerical inversion experiments with the SWD sources located along a plausible well-trajectory with different source settings through a synthetic model. These SWD sources are supplemented by explosive sources and multicomponent receivers at the surface, simulating a conventional surface acquisition geometry. The subsurface model and SWD source properties are recovered and analyzed. After adding SWD data, both the inversion of physical elastic properties and source mechanisms get considerably enhanced, even in the cases where low frequencies are missing; the inversion also shows preferences on the features of the sequence of SWD sources along the trajectory. This model-source inversion algorithm also indicates the potential to simultaneously estimate the anelastic properties and trajectory deviation while drilling. The analysis suggests that, in principle, SWD participation improves the accuracy of FWI models, and source information can also be acquired. However, further studies are required to provide a more comprehensive representation of the SWD sources.

INTRODUCTION

Full-waveform inversion (FWI) is a set of methodologies in which seismic data are used to estimate the physical properties of the Earth. By iteratively minimizing a misfit function measuring the difference between synthetically modeled and experimentally recorded data, the subsurface distributions of elastic properties and other relevant unknowns are updated to produce high-resolution model estimates (Tarantola, 1984, 2004; Virieux and Operto, 2009; Brittan et al., 2013). In applying FWI to field data, several well-known practical issues and challenges arise, which can strongly affect the accuracy of the inverted models (Brossier et al., 2009; Fichtner, 2011; Métivier et al., 2017; Singh et al., 2018; Pan et al., 2019; Aragao and Sava, 2020). An important example is acquisition geometry. In particular, the necessarily limited spatial sampling and aperture of the seismic experiment (Jannane et al., 1989; Mothi et al., 2014; Kerrison et al., 2021). Seismic rays tend to bend toward high-velocity zones, such as salt bodies, and away from low-velocity zones, such as overpressure regions (Cheadle et al., 1991; Kazemi et al., 2020), etc. In general, the complicated and non-uniform ray paths associated with incomplete acquisition and complex heterogeneous media introduce shadow zones, regions of the geological medium which are poorly constrained. At best, physical properties in those regions are inaccurately recovered

unless additional a priori subsurface information is used to fill in the gaps in ray path coverage (Tiwari et al., 2018; Liu et al., 2020). The unavailability of low and intermediate model wavelengths from datasets associated with short-offset surface acquisitions is perhaps the best-known issue arising from acquisition limitations — wide-aperture acquisition, which increases the number of overlapping ray paths, is essential in these cases (Virieux and Operto, 2009; Vigh et al., 2021).

A clear, but often practically difficult, solution is to include additional, e.g., subsurface, sources or receivers in the seismic survey, which introduce unique ray paths supporting the estimation of essential model components. Acquisition geometries which include sources or receivers in the subsurface, for instance, cross-well (Pratt et al., 1996; Pratt, 1999; Pratt and Shipp, 1999) and vertical seismic profile, or VSP (Pan et al., 2018; Podgornova et al., 2018; Eaid et al., 2022), naturally supply these, and lead to different, and in some respects better, FWI model estimates and convergence properties. Generally, improvements are tied to the appearance of ray paths that interact with the medium through transmission-like geometries; in reflection surveys, these are, for the most part, limited to diving waves, which explains the necessity for long offsets (Virieux and Operto, 2009; Brittan and Jones, 2019).

Seismic-while-drilling (SWD) is a longstanding auxiliary tool in exploration and monitoring seismology (e.g., Sheppard and Lesage, 1988; Rector and Hardage, 1992; Miranda et al., 1996; Naville et al., 2004; Poletto and Miranda, 2004), wherein the drill bit acts as a seismic source, and sensors arrayed in a range of possible geometries produce an experiment similar to a reverse VSP (Khaled et al., 1996; Miranda et al., 1996). The approach is attractive because it generates a field of important extra seismic information in real-time without interrupting drilling processes (Poletto and Miranda, 2004). SWD has attracted renewed interest in recent years, taking advantage of advances in the understanding of drill-string dynamics and the use of neural networks for data analysis (e.g., Auriol et al., 2021). It has been pointed out that the introduction of SWD ray paths, which begin at the drill bit and end at surface or borehole receivers, can, in principle, constrain velocity models (Bertelli and di Cesare, 1999), and that this could further impact imaging (Kazemi et al., 2018) and FWI (Kazemi et al., 2021) by partially addressing the issues discussed above.

Additionally, using SWD data to complement other seismic data, ostensibly in support of imaging or FWI, feeds back into the problem of drilling optimization. A drilling program is naturally de-risked when better estimates of physical parameters near the drill string are available (Poletto et al., 2003; Martinez et al., 2020). Reducing uncertainty in, for instance, locations of formation tops, and heterogeneities in general within a complex stratigraphy, is relevant to geohazard avoidance, e.g., zones of high pore pressure. Further, near-real-time updating of drilling parameters requires accurate seismic velocity estimates within the formations interacting with the drill bit (Auriol et al., 2021). Models deriving from FWI would, in principle, address both of these issues.

The potential of SWD as an enabler of seismic imaging and inversion was first discussed by Bertelli and di Cesare (1999), who proposed using velocity information from real-time reprocessing of the SWD dataset to adjust and continuously refine the velocity model for migration. Rocca et al. (2005) developed a migration approach wherein a circu-

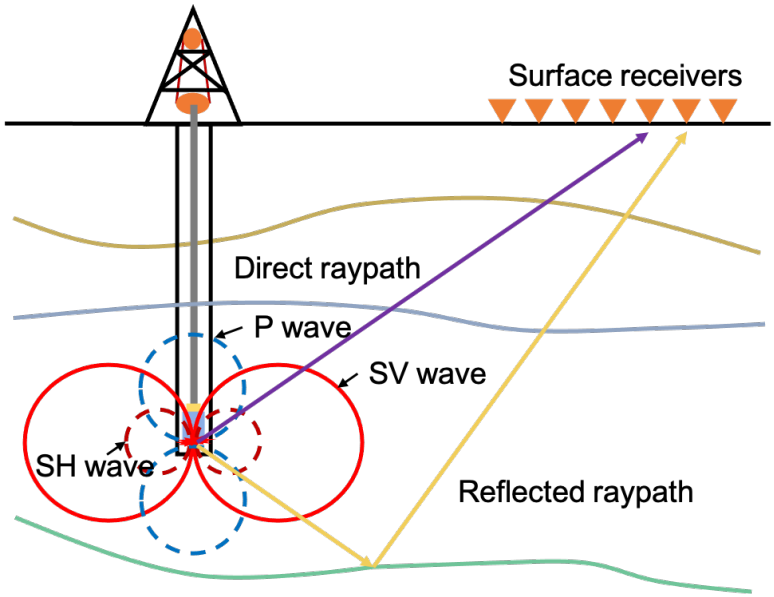

FIG. 1. Schematic figure of the radiation patterns of SWD sources (modified after Rector and Hardage (1992)).

lar line of receivers is settled to apply the 3D migration in the angular frequency domain, and this method successfully recovered the position of reflectors in a horizontally layered medium. Vasconcelos and Snieder (2008) applied the deconvolutional interferometry in SWD field data to provide an interferometric image of a fault zone at depth within the study area, and Poletto et al. (2012) tested SWD with seismic interferometry and migration to map the geothermal field around wells. Kazemi et al. (2018) formulated an illumination compensation for imaging of surface data using SWD data processed with a sparse multichannel blind deconvolution (SMBD) algorithm, originally built for other applications (Kazemi and Sacchi, 2014). Similar arguments led to the formulation of a two-stage sequential SWD-FWI algorithm, in which inversion of data from SWD sources was followed by inversion from conventionally-acquired surface data (Kazemi et al., 2021). These studies provide strong evidence that the ray paths associated with SWD do have a marked impact on model estimation when used in combination with other data sets. However, the assumption of acoustic wave physics, the estimation of a single unknown model parameter class (i.e., scalar acoustic P-wave velocity), and the assumption that the radiation characteristics of the drill bit are known (or can be accommodated through preprocessing) are all idealizations making proper feasibility analysis difficult. Borehole inclination and azimuth change the vertical and horizontal components of the SWD signal. For instance (see Figure (1)), drill bit radiation patterns have strong directionality features, and wide ranges of surface receiver locations are likely to be sensitive primarily to S-wave energy. The SWD signal is thus inherently elastic. Further, the complicated interaction of the continuously-radiating source drill-bit and the formation rock will induce strong modeling errors in an FWI scheme formulated with a static, known, and simply-radiating point source.

THEORY

In this paper, seismic data are regarded as measurements of a wavefield that has propagated through an unknown distribution of elastic medium properties as the result of a localized source with a known (or pre-determined) position, a known (or pre-determined) source wavelet, and an unknown moment tensor. A candidate set of these known and unknown parameters is used to simulate frequency-domain seismic data, and those simulations are used to drive a modified full-waveform inversion algorithm, as follows.

Forward modeling

We employ a finite-difference solution of the 2-D isotropic viscoelastic wave equation in the frequency domain (Pratt, 1990; Brossier et al., 2010), and 2-D moment tensors (e.g., Aki and Richards, 2002; Vavrycuk, 2005; Tape and Tape, 2013) to represent source radiation. The viscoelastic wave equations are

$$\begin{cases} \omega^2 \rho u_x + \frac{\partial}{\partial x}\left[\tilde{\lambda}\left(\frac{\partial u_x}{\partial x}+\frac{\partial u_z}{\partial z}\right)+2\tilde{\mu}\frac{\partial u_x}{\partial x}\right]+\frac{\partial}{\partial z}\tilde{\mu}\left(\frac{\partial u_z}{\partial x}+\frac{\partial u_x}{\partial z}\right)+f_x=0, \\ \omega^2 \rho u_z + \frac{\partial}{\partial z}\left[\tilde{\lambda}\left(\frac{\partial u_x}{\partial x}+\frac{\partial u_z}{\partial z}\right)+2\tilde{\mu}\frac{\partial u_z}{\partial z}\right]+\frac{\partial}{\partial x}\tilde{\mu}\left(\frac{\partial u_z}{\partial x}+\frac{\partial u_x}{\partial z}\right)+f_z=0, \end{cases} \tag{1}$$

where ω is the angular frequency, ρ is the density, u_x and u_z are displacement components, and f_x and f_z are the source terms in the horizontal and vertical directions, respectively; $\tilde{\lambda}$ and $\tilde{\mu}$ are complex Lamé parameters and are frequency-dependent and related to quality factors Q_p and Q_s:

$$\begin{cases} \tilde{\lambda} = V_p^2\left\{1+\frac{1}{Q_p}\left[\frac{1}{\pi}\log\left(\frac{\omega}{\omega_0}\right)+\frac{i}{2}\right]\right\}^2\rho-2\tilde{\mu}, \\ \tilde{\mu} = V_s^2\left\{1+\frac{1}{Q_s}\left[\frac{1}{\pi}\log\left(\frac{\omega}{\omega_0}\right)+\frac{i}{2}\right]\right\}^2\rho. \end{cases} \tag{2}$$

The fields u_x and u_z are discretized onto a square grid, and the derivatives are approximated using standard methods (e.g., Pratt, 1990). f_x and f_z are the source terms in the horizontal and vertical directions, respectively. Wavefields are excited at particular positions (i.e., grid cell locations). Source radiation patterns are simulated with general 2-D isotropic moment tensors $\mathbf{M}$, which have 3 independent components M_{11}, M_{12}, and M_{22}, with M_{ij} representing the derivative in the jth direction of the ith component of displacement. The M_{ij} values lie between -1 to 1.

To include moment tensor source representations, it is necessary to approximate derivatives in the vicinity of the source in the finite-difference model (Keating and Innanen, 2020). Figure (2) illustrates our first-order difference approach to calculating source-related derivatives. For a point source located midway between two finite-difference cell centers (Figure (2)-(a)), the finite difference approximation of $M_{11} = 1$ can be represented with differences formed between two adjacent cells by summing with weights $\frac{-1}{\Delta x}$ and $\frac{1}{\Delta x}$. If the source position is not equidistant between finite-difference cell centers, which is the general case shown by Figure (2)-(b), we use three continuously-weighted members to approximate the first-order spatial derivatives. The finite-difference weights used for a source location between two finite-difference grid lines is a weighted average of the amplitudes used for a source at either of the bounding grid lines, as shown in Figure (2)-(b). Extending

this concept to the 2-D case, the finite difference approximation can be defined by weighting between intersections of nine grid cells in a small surrounding region. Specifically, we define stencil variables with indices of the four cells for a point source shown by the red dot in Figure (3). The top-right cells (0, $-z$, $+x-z$, $+x$) make the NE stencil, and the SE, SW, and NW stencils can be represented by the bottom-right, bottom-left, and top-left four-cell sections following the same indexing rule.

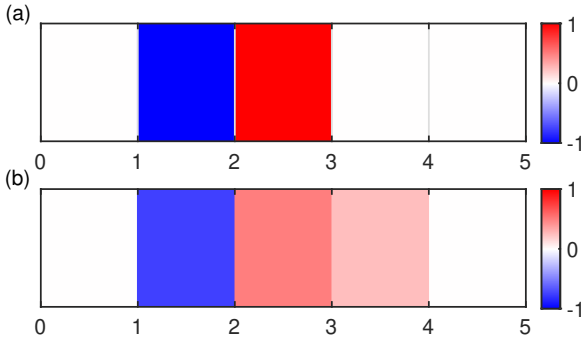

FIG. 2. Scaled weights for approximating an example of $M_{11} = 1$ in one dimension. (a) weights for source location $x = 2$. (b) weights for source location $x = 2.25$.

$-x-z$	$-z$	$+x-z$
$-x$	●	$+x$
$-x+z$	$+z$	$+x+z$

FIG. 3. Stencil variables definition. The red dot in the center cell is the source location.

With the stencils well defined, the finite difference approximation of moment tensors can be defined on each of the four stencils. In our formulation, f_x and f_z in equation (1) are expressed by nine grid cells surrounding an arbitrary source position considering a weighted summation of moment tensor components in each stencil based on the specific locations of a source within the center cell:

$$\begin{cases} f_x = \sum_{\mathbf{s}} \mathbf{w}\left(\mathbf{s}\right)\left[M_{11} w_{dx}\left(\mathbf{s}\right) + M_{12} w_{dz}\left(\mathbf{s}\right)\right], \\ f_z = \sum_{\mathbf{s}} \mathbf{w}\left(\mathbf{s}\right)\left[M_{12} w_{dx}\left(\mathbf{s}\right) + M_{22} w_{dz}\left(\mathbf{s}\right)\right], \end{cases} \tag{3}$$

where $\mathbf{w}\left(\mathbf{s}\right)$ is the spatial weighting term considering the skewing of a point source to the mid of a grid cell. $\mathbf{s}$ is an indexing vector containing four indices of a stencil that can be chosen from NE-SW-SW-NW. $w_{dx}\left(\mathbf{s}\right) = 1$ or -1 when $\mathbf{s}$ contains eastward (right) or westward (left) direction; $w_{dz}\left(\mathbf{s}\right) = 1$ or -1 when there is southward (down) or northward (up) in the stencils.

This treatment makes it possible to precisely represent a point source in arbitrary locations. Figure (4) shows an approximation example based on the assumption of $M_{11} = 1$,

while it is also applicable for a point source with a more general moment tensor combination. Small changes in the source locations correspond to a small re-weighting of the source term values. In such a case, the gradient of the objective function with respect to these variables is well defined by our approximation.

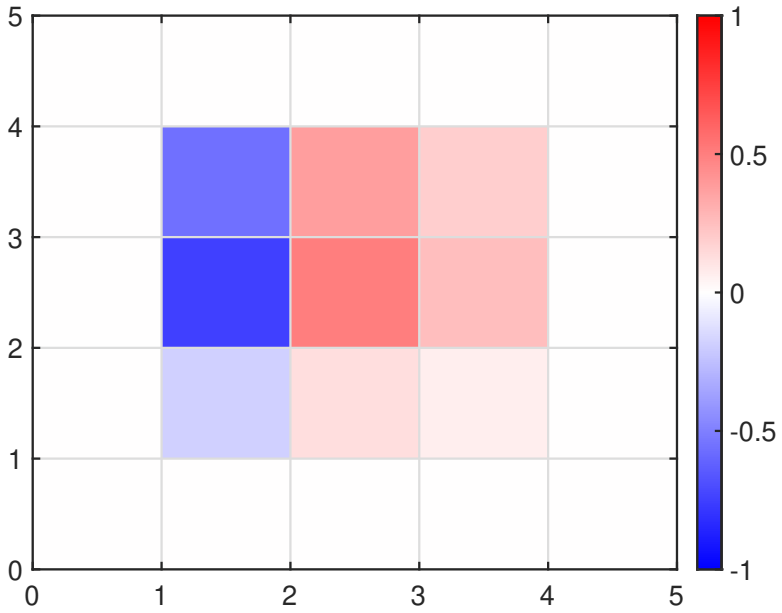

FIG. 4. Scaled weights for approximating an example of $M_{11} = 1$ in two dimension with source location $x = 2.25$ and $z = 2.25$.

2-D frequency-domain FWI

Inversions are carried out through 2-D frequency-domain elastic FWI, optimized with a truncated-Newton approach following Keating and Innanen (2020), who built on the formulation of Pratt (Pratt, 1990, 1999). In the frequency domain, the problem is to obtain

$$\text{argmin}_{\mathbf{x}}\Phi\left(\mathbf{x}\right) = \text{argmin}_{\mathbf{x}}\sum_{j=1}^{N_\omega}\sum_{k=1}^{N_s}\frac{1}{2}\mathbf{R}\mathbf{u}_{j,k} - \mathbf{d}_{j,k}{}_2^2, \text{ s.t. } \mathbf{S}(\mathbf{x})\mathbf{u} = \mathbf{f}, \tag{4}$$

where $\mathbf{x}$ is a vector of inversion variables (which will ultimately comprise both subsurface and source unknowns), ω is the frequency, s denotes the source index, $\mathbf{R}$ is the sampling matrix representing the measurements of receivers, $\mathbf{u}$ is the discretized wave field due to the fixed source, $\mathbf{d}$ is the vector observed data between a source-receiver pair, $\mathbf{S}$ is the finite-difference modeling operator, and $\mathbf{f}$ is the source term. In this paper, we assume that the wavefield only has one source and frequency component for simplicity.

The adjoint state method (e.g., Plessix, 2006; Fichtner et al., 2008) is used to determine the gradient through a combination of forward and backward propagated wavefields, the latter of which has the residual wavefield as the source. We start by formulating the Lagrangian of this problem:

$$L\left(\mathbf{x}\right) = \frac{1}{2}\mathbf{R}\mathbf{u} - \mathbf{d}_2^2 + \left\langle \mathbf{S}\left(\mathbf{x}\right)\mathbf{u} - \left(\mathbf{f}_R + i\mathbf{f}_I\right), \lambda \right\rangle, \tag{5}$$

where λ is a vector of Lagrange multipliers, $\mathbf{f}_R$ and $\mathbf{f}_I$ are the real and imaginary parts of the source term $\mathbf{f}$. $\langle \cdot, \cdot \rangle$ represents the inner product. We consider a wavefield $\overline{\mathbf{u}}$ that satisfies the wave equation such that $L\left(\overline{\mathbf{u}}\right) = \Phi$. By choosing $\overline{\lambda}$ that satisfies $\frac{\partial L}{\partial \overline{\mathbf{u}}} = 0$, the complicated calculation of $\frac{\partial \overline{\mathbf{u}}}{\partial \mathbf{x}}$, namely the Jacobian matrix can be avoided. Such $\overline{\lambda}$ can be solved through a backpropagation process in which data residual is considered the source term. The derivative of the objective function with respect to any inversion variable is then given by:

$$\frac{\partial \Phi}{\partial \mathbf{x}} = \frac{\partial L\left(\overline{\mathbf{u}}, \overline{\lambda}\right)}{\partial \mathbf{x}}. \tag{6}$$

The Hessian matrix is required in the optimization procedure to accelerate the convergence and improve the resolution of the inversion. However, the full Newton approach is not recommended due to the high computational demand (Pratt et al., 1998), so some alternative methods are developed and tested. In convention, Pratt et al. (1998) preconditioned the steepest-descent or conjugate-gradient by the diagonal components of the approximate Hessian. Shin et al. (2008) took advantage of the pseudo-Hessian, and Brossier et al. (2009) applied a quasi-Newton method based on the LBFGS algorithm (Nocedal and Wright, 2006). The iterative process in this approach estimates the curvature information in the Hessian matrix from a limited number of recently stored vectors. This approach exploits the computer capacity and extracts as much information from the Hessian matrix. This paper uses such an approach that efficiently truncates the Gauss-Newton Hessian calculation with several fixed iterations (Métivier et al., 2013). The Truncated Gauss-Newton method is based on the Gauss-Newton approximation of Hessian which keeps the first-order part of it and thus obtains the diagonal part of the Hessian matrix (Nash, 2000).

Hessian-vector products involving $\mathbf{H}$ are also derivable through similar argumentation with the calculation of the gradient (Métivier et al., 2013, 2015; Xing and Zhu, 2020). From the FWI objective function defined in equation (4), the Gauss-Newton Hessian can be given by:

$$\mathbf{H}_{GN} = J^{\dagger}\mathbf{R}^T\mathbf{R}J, \tag{7}$$

where J is the Jacobian matrix, and $\dagger$ denotes the conjugate transpose. Following the same concept of the adjoint state method, the costly calculation of the Jacobian matrix in the Gauss-Newton Hessian can also be avoided. We consider such a Lagrangian:

$$\tilde{L} = \langle \mathbf{u}\left(\mathbf{x}\right), \mathbf{w} \rangle + \langle \mathbf{S}\left(\mathbf{x}\right)\mathbf{u} - \left(\mathbf{f}_R + i\mathbf{f}_I\right), \mu \rangle, \tag{8}$$

where $\mathbf{w} = \mathbf{R}^T\mathbf{R}J\mathbf{v}$, and $\mathbf{v}$ is an arbitrary vector.

Referring to the gradient calculation with the adjoint state method, similarly, the Lagrange multiplier $\overline{\mu}$ satisfies:

$$\mathbf{S}^{\dagger}\overline{\mu} + \mathbf{w} = 0, \tag{9}$$

However, it is challenging and thus not prioritized to directly solve for $\mathbf{w}$ because the Jacobian matrix J is contained. Alternatively, we calculate the product of J with the vector

$\mathbf{v}$ through consideration of the derivative of the forward problem with respect to variables x_p multiplied by vector elements v_{x_p} (Métivier et al., 2013; Keating and Innanen, 2020):

$$\frac{\partial \left(\mathbf{S}\mathbf{u} - \mathbf{f}\right) v_{x_p}}{\partial x_p} = 0. \tag{10}$$

This allows us to acquire $\mathbf{w}$ and thus derive the Lagrange multiplier $\overline{\mu}$ in equation (9). The Gauss-Newton Hessian vector product $\mathbf{H}_{GN}\mathbf{v}$ can be then shown by $\frac{\partial \tilde{L}}{\partial \mathbf{x}}$.

Incorporation of source unknowns

Let us now suppose that the model unknown vector $\mathbf{x}$ is made up of medium property unknowns, contained in the vector $\mathbf{m}$, and source unknowns, contained in the real vectors $\mathbf{f}_R$ and $\mathbf{f}_I$, such that the full source vector in equation (4) is $\mathbf{f} = \mathbf{f}_R + i\mathbf{f}_I$ (also shown explicitly in equation (5) and equation (8). Equation (6) can be separated as:

$$\frac{\partial L}{\partial m_p} = \left\langle \frac{\partial \mathbf{S}}{\partial m_p}\overline{\mathbf{u}}, \overline{\lambda} \right\rangle, \tag{11}$$

where p labels the pth component of model parameters.

$$\frac{\partial L}{\partial f_{R_p}} = -\mathfrak{Re}\left(\overline{\lambda_p}\right), \tag{12}$$

and

$$\frac{\partial L}{\partial f_{I_p}} = \mathfrak{Im}\left(\overline{\lambda_p}\right), \tag{13}$$

$\mathbf{f}_R$ and $\mathbf{f}_I$ both have large dimensionality with a number of elements equal to the number of points in the wavefield used in forward modeling multiplied by the number of the unknown sources considered, so it is necessary to have more restrictions on source-related variables. Consider a variable $\mathbf{f}_r$ that controls the moment tensors or position of a point source. The derivative of the objective function with respect to such a variable is an extension of the derivative with respect to the force term:

$$\frac{\partial \Phi}{\partial \mathbf{f}_r} = \sum_p \left[-\mathfrak{Re}\left(\overline{\lambda}_p\right) \frac{\partial f_{R_p}}{\partial \mathbf{f}_r} + \mathfrak{Im}\left(\overline{\lambda}_p\right) \frac{\partial f_{I_p}}{\partial \mathbf{f}_r} \right], \tag{14}$$

where the first part within the summation on the right-hand side is the derivative of the real component of the source term with respect to $\mathbf{f}_r$, and the second part is the derivative of the imaginary component of the source term with respect to $\mathbf{f}_r$.

This concept also holds in the Hessian-vector products. Using the relation in equation (10), it can be shown that

$$\mathbf{S}\left(J_{\mathbf{m}}\mathbf{v}_{\mathbf{m}}\right) = -\mathbf{u}\sum_p \left(\frac{\partial \mathbf{S}}{\partial m_p} v_{m_p} \right), \tag{15}$$

$$\mathbf{S}\left(J_{f_R}\mathbf{v}_{f_R}\right) = \mathfrak{Re}\left(v_{f_{R_p}}\right), \tag{16}$$

and More specifically

$$\mathbf{S}\left(J_{f_R}\mathbf{v}_{f_R}\right) = \mathfrak{Im}\left(v_{f_{I_p}}\right), \tag{17}$$

where v_{m_p} is the element of $\mathbf{v}$ corresponding to the pth element of $\mathbf{m}$, $v_{f_{R_p}}$ is the element corresponding to the pth element of $\mathbf{f}_R$ and $v_{f_{I_p}}$ is the element corresponding to the pth element of $\mathbf{f}_I$.

NUMERICAL EXAMPLES

The numerical tests in this section are based on synthetic models to evaluate the performance and investigate the potential of combining seismic-while-drilling datasets with simultaneous model-source FWI. Figure (5) shows the true and initial models. One of the major advantages of our inversion is the intervention of additional sources can provide feasible information on the subsurface anelastic models, so the starting model for our inversion is based on the assumption that there is less prior information available. The whole model size is 300 by 150 grid points in x and z directions, with a 20-meter interval.

We assume that (1) the drill can be treated as if it occupies a discrete sequence of quasi-static positions along the drill trajectory, (2) the radiation patterns of the SWD sources are represented by independent and general moment tensors, which means force couples can approximate the drill-bit-rock interaction; the problem of transformation of SWD signals into useable seismic data has been discussed by Kazemi et al. (2021), and (3) the SWD data can be analyzed into the discrete FWI frequencies we select below.

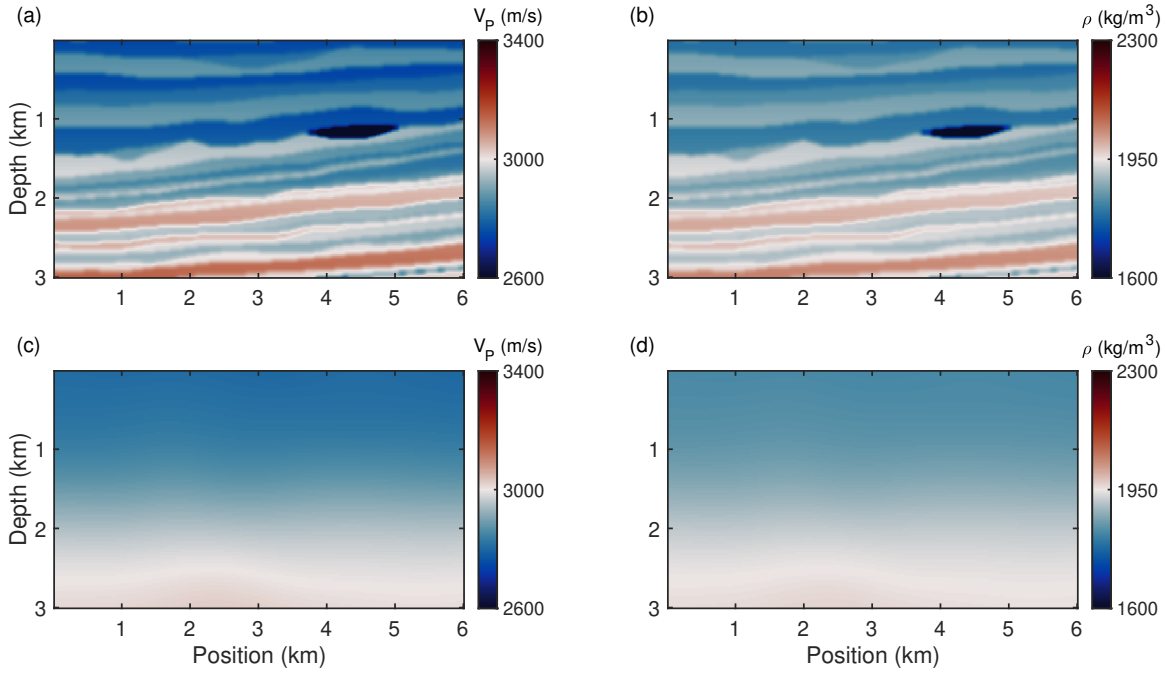

FIG. 5. True and initial subsurface properties of the synthetic models. (a) True P-wave velocity model. (b) True density model. (c) Initial P-wave velocity model. (d) Initial density model.

The multi-scale approach is used throughout this paper. We subsequently update the model with 10 frequency bands, each containing 12 sub-frequencies. The starting frequencies of every band are set to 1 Hz, while the ending frequencies linearly increase from 2 Hz (for the first band) to 15 Hz (for the last one). 20 inner iterations are used for approximation of the inverse Hessian in the truncated Gauss-Newton approach, and 3 outer iterations are set to update each band's model.

Simultaneous inversion for subsurface parameters and moment tensors

This section estimates the V_P, density, and radiation patterns together while keeping the unknown source positions fixed. Two acquisition geometries are considered here: for surface acquisition, there are 72 explosive sources with a gap of 2 grid points and 144 multi-component receivers with a 1-grid interval; for source unknowns, various distributions are designed to test the inversion in different settings. Specifically, we carry out the inversion tests where the source number, trajectory inclination, and drilling path extension are taken into account separately.

As the transmissive ray paths provide the inversion with profound contribution, it is necessary for us to apply some constraints to the SWD-generated datasets to ensure our tests are closer to real situations where there is little direct intervention from the transmission. We scaled the amplitude of SWD datasets to be half as the surface data. We added the Gaussian noise with 10 dB and 5 dB signal-to-noise ratios (SNRs) to data generated from isotropic and drilling sources.

Source number test

While introducing the additional ray paths to improve the FWI, the increased nonlinearity brought by source unknowns should also be evaluated. In this set of experiments, we investigate the impact of unknown source numbers along a drilling trajectory of a fixed length. Figure (6) shows the schematic acquisition geometry of the source number test. Our main inversion focus is the triangle abnormaly indicated by the black dashed rectangle in the model's right half. The horizontal size of the model is considerably larger than the target inversion zone based on the following two considerations: (1) in practical applications, there is usually a distance between the drilling sites and the surface sensors; (2) the far-field assumption should be satisfied in representing force-couple-defined sources with a point approximation (Aki and Richards, 2002). The surface acquisition, as shown by the red and green markers, covers the surface of the inversion target. A drilling trajectory is then added in the deeper section of the left-hand side of our model, and the blue stars indicate unknown sources. The drilling site on the ground has around 1.5 kilometers offset from the ground receivers, and various SWD sources are arranged along a deviated trajectory of 900 meters. We have tested the cases where $N_S = 10, 15, 20, 25,$ and 30. Random moment tensors set the initial and true radiation patterns for each unknown independent point source in a range of -1 to 1.

We first show the results of subsurface properties with the surface-only acquisition in Figure (7) as a baseline inversion for further comparison with the cases where SWD sources adjoint. The estimation of both P-wave velocity and density is very crude, as shown by the

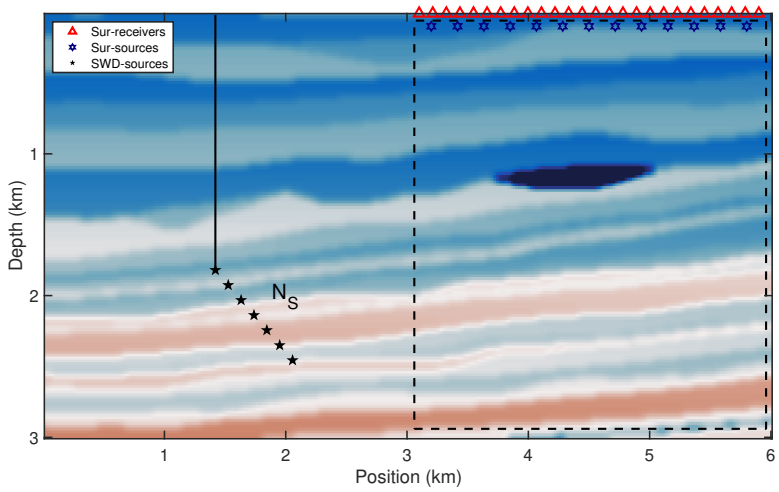

FIG. 6. Schematic acquisition system in source number test.

indistinct structures in the recovered models. The right-hand side portions of the models are slightly updated, but the other parts where no extra source exists are poorly recovered. For the misfit calculation, we use the root mean square error normalized by the difference between the maximum and minimum values of the true data for the misfit:

$$NRMSE = \frac{RMSE}{max\left(data_{true}\right) - min\left(data_{true}\right)}. \tag{18}$$

The high NRMSE values shown in Figure (7) quantitatively suggest unsatisfactory inversions with only surface acquisition settings.

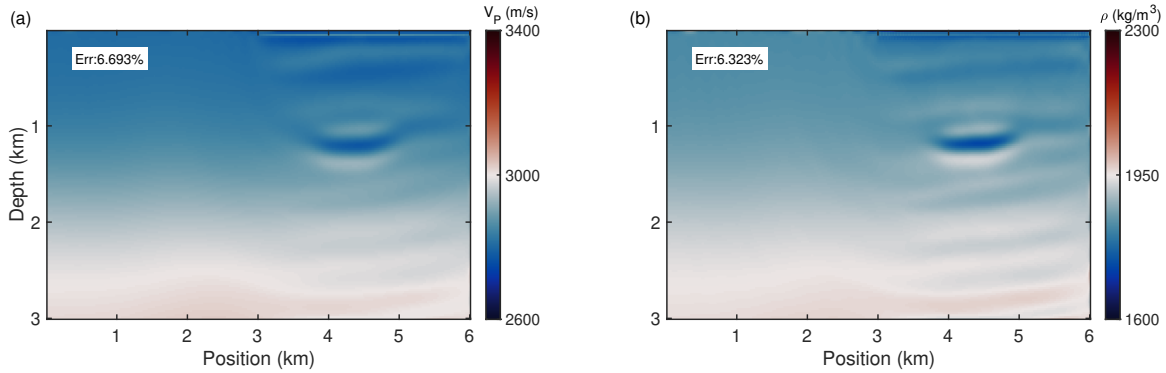

FIG. 7. Inversion of V_P and ρ with surface acquisition. (a) V_P inversion with surface acquisition. (c) ρ inversion with surface acquisition.

The inversion results in Figure (8) show a profound enhancement when including the SWD data, even though there are only a few drilling sources involved (Figure (8) (a) and (b)). The abnormaly in the target inversion zone is well recovered, and the intermediate medium between the extra sources to the receivers is also fairly estimated. The recovery for both V_P and density shows a positive correlation between the improvement and the source number, as shown by larger extensions of the lower high abnormalies and the gradually reduced error terms.

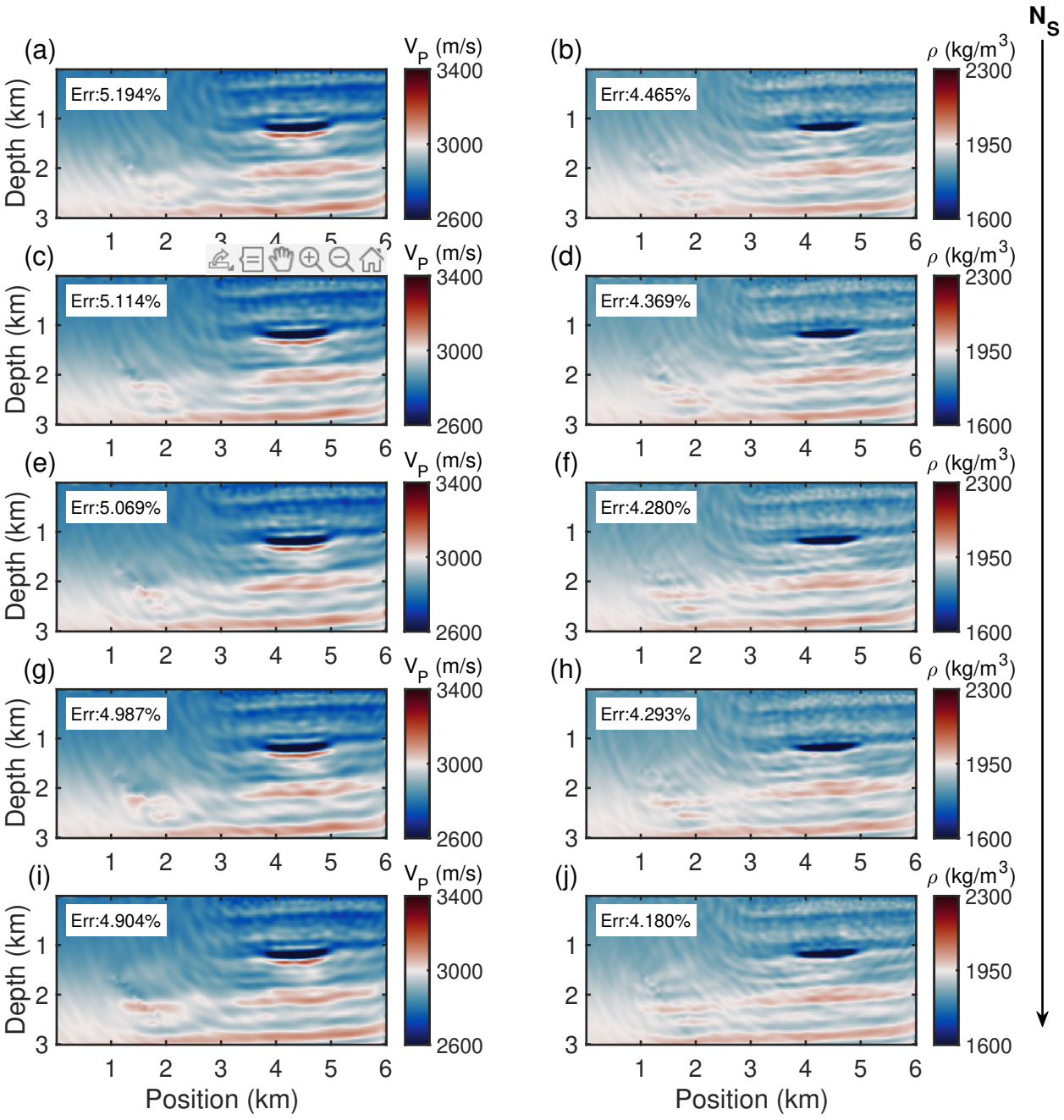

FIG. 8. Inversion of V_P and ρ with surface and SWD acquisitions with different source number. The black arrow denotes the gradual increment of N_S. (a)-(b) inversion with $N_S = 10$. (c)-(d) inversion with $N_S = 15$. (e)-(f) inversion with $N_S = 20$. (g)-(h) inversion with $N_S = 25$. (i)-(j), inversion with $N_S = 30$.

We use 3 vertical profiles in the x-position of 3.6, 4.6, and 5.6 kilometers to quantify the improvement when combining the SWD data. The comparisons are shown in Figure (9), where the black lines are from true models, the dark green lines are from the baseline models, and S_1-S_5 denote five cases in which N_S increases from 10 to 30. The NRMSE is also calculated in each profile. The profiles of all the cases are much more close to the true cross-sections. In the closer profiles, we get the best velocity inversion when the source number is 20, but the density profile shows the best result when the source number is 30. Things are similar in further cases, as more sources do not mean better results in these local profiles.

The moment tensor inversion results, however, do not necessarily change in accordance with the number of unknown sources. The cross plots in Figure (10) generally show good convergence in all cases. Combining the inversions of models and source terms, it is reasonable to infer that the contribution from the increase of SWD sources outweighs the risk of more significant nonlinearity introduced by more unknown radiation patterns.

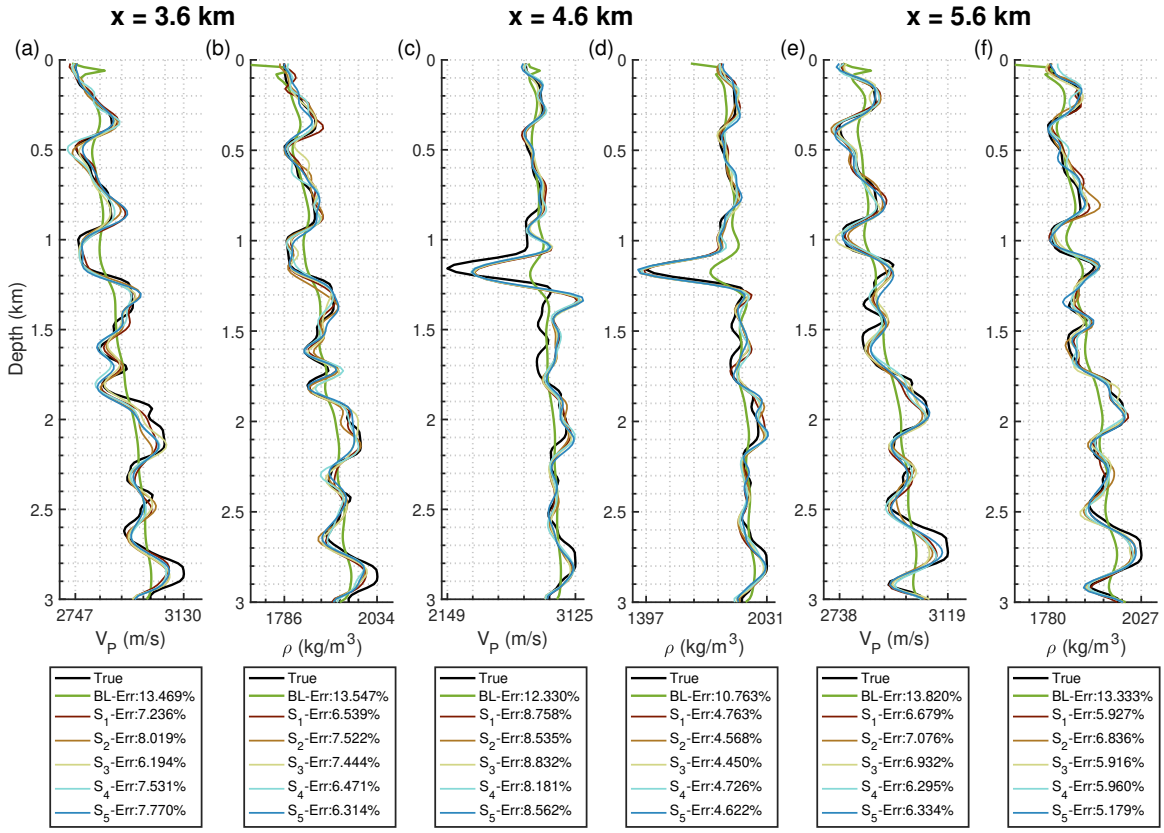

FIG. 9. Profiles in source number test. (a), (c), and (e) are P-wave velocity cross-sections, while (b), (d), and (f) are density cross-sections.

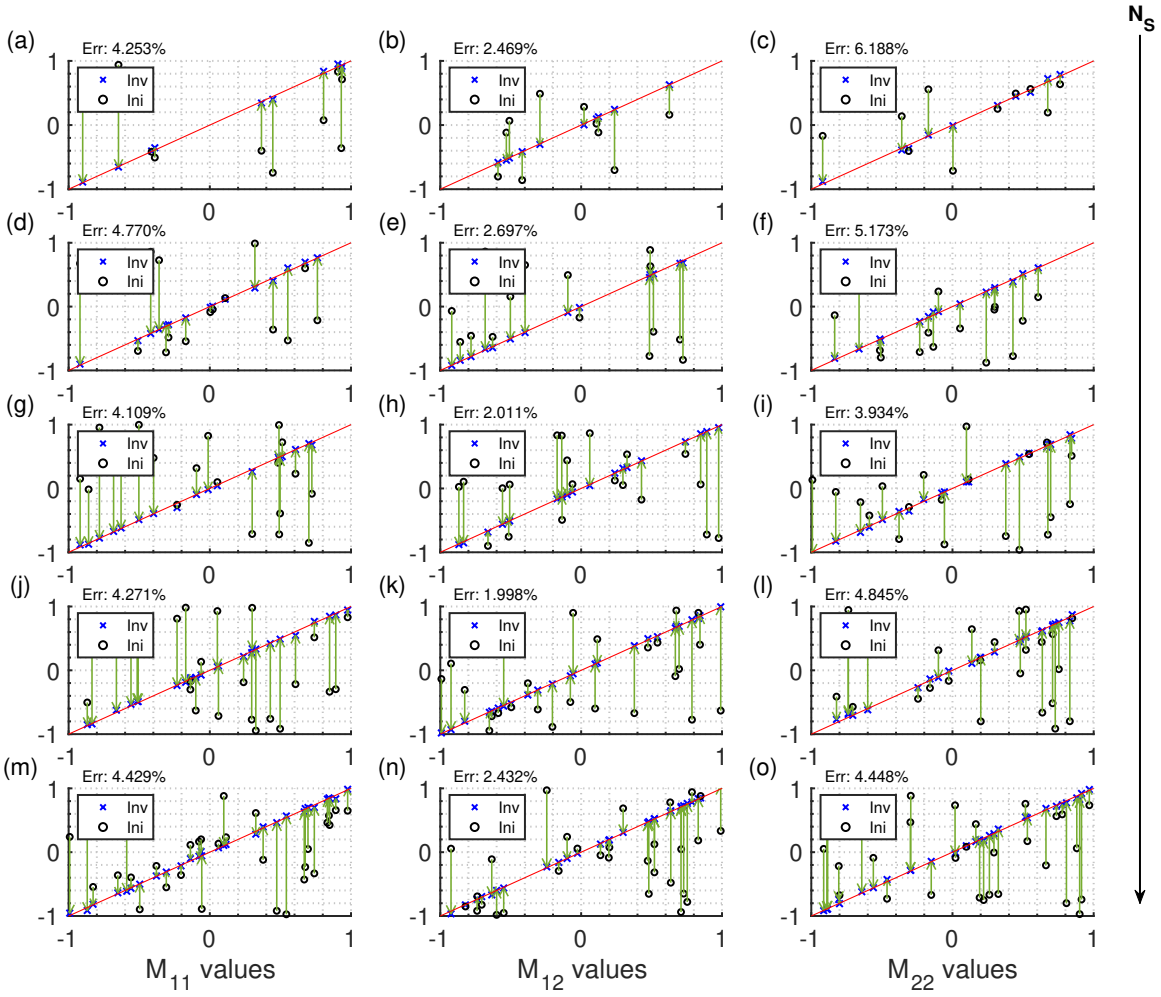

FIG. 10. Inversion of moment tensors. The black arrow denotes the gradual increment of N_S, and the green arrows are from initial values to estimated values. (a)-(c) $N_S = 10$. (d)-(f) $N_S = 15$. (g)-(i) $N_S = 20$. (j)-(l) $N_S = 25$. (m)-(o) $N_S = 30$.

Trajectory inclination test

This test examines the influence of how much the drilling trajectory deviates from vertical. We implement a drilling path with a fixed length of 900 m, same as the previous test, with 30 sources with unknown moment tensor settings. The angle θ in Figure (11), as the only variable in this section, varies from $0°$ (vertical) to $90°$ (horizontal), with an increment of $22.5°$.

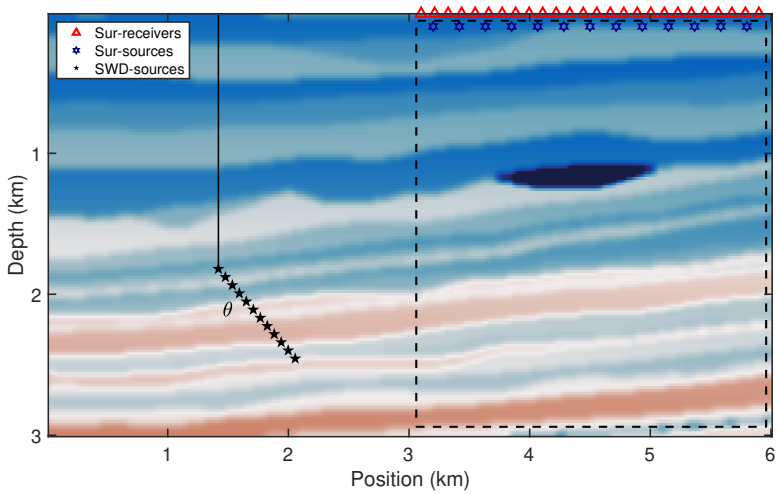

FIG. 11. Schematic acquisition system in trajectory inclination test.

As shown in Figure (12), the layered structures and the main abnormaly of both the P-wave velocity and density models are depicted after the FWI, emphasizing the help from additional sources when compared to the baseline inversion. The error is relatively lower in inversions with a horizontal drilling path, and the high abnormalies are better reconstructed because of a higher horizontal resolution. The profiles in Figure (13) also display steady FWI results with different deviations, and all of the cases with extra SWD sources are better consistent with the true values.

The overall NRMSE gets smaller when the trajectory deviates and reaches its lowest in the case where $\theta = 20°$, but enlarged again as it becomes closer to horizontal. Generally, the moment tensor inversions are consistent.

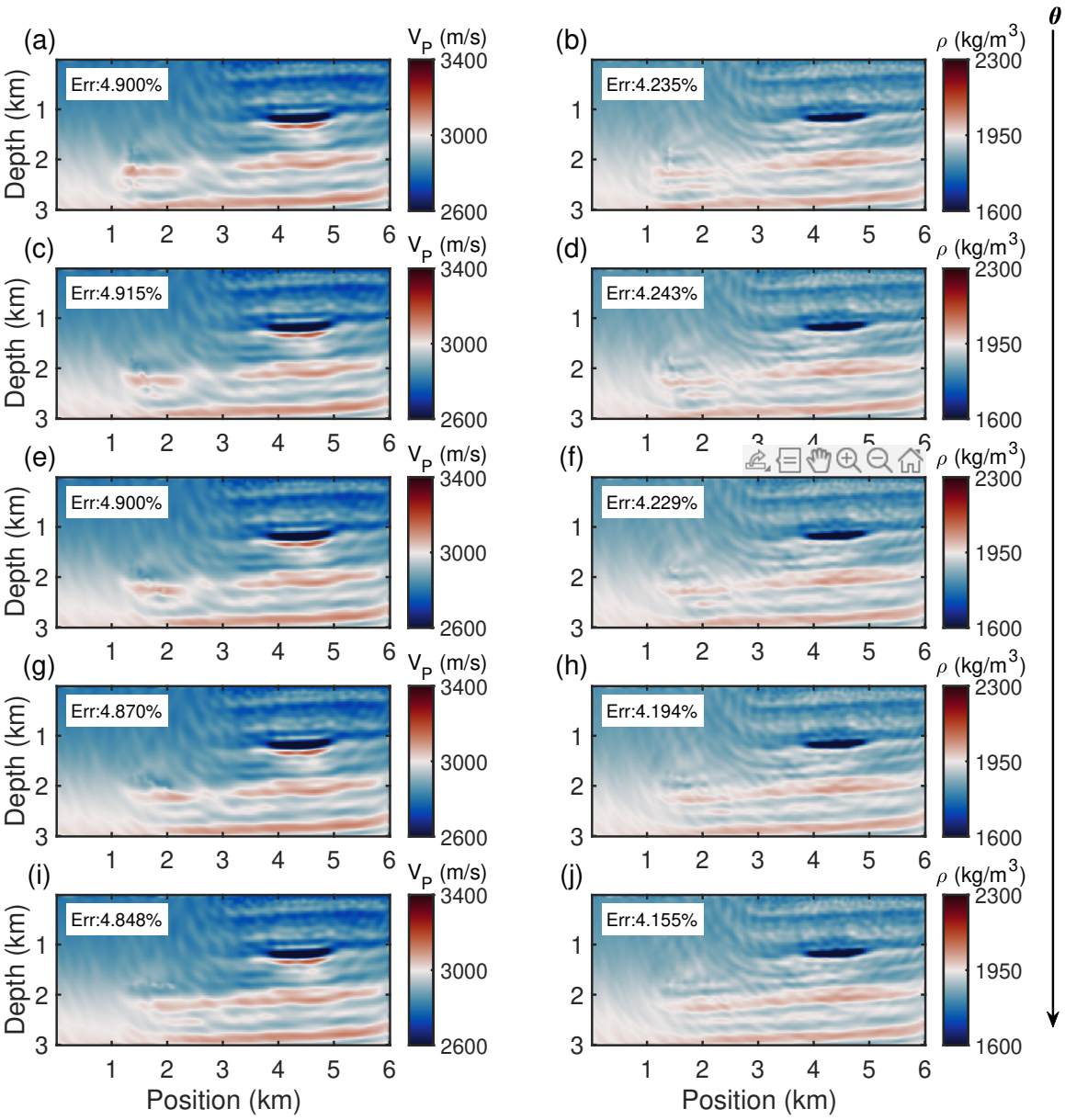

FIG. 12. Inversion of V_P and ρ with surface and SWD acquisitions with different trajectory inclinations. The black arrow denotes the gradual increment of θ. (a)-(b) inversion with $\theta = 0°$. (c)-(d) inversion with $\theta = 22.5°$. (e)-(f), inversion with $\theta = 45°$. (g)-(h) inversion with $\theta = 67.5°$. (i)-(j) inversion with $\theta = 90°$.

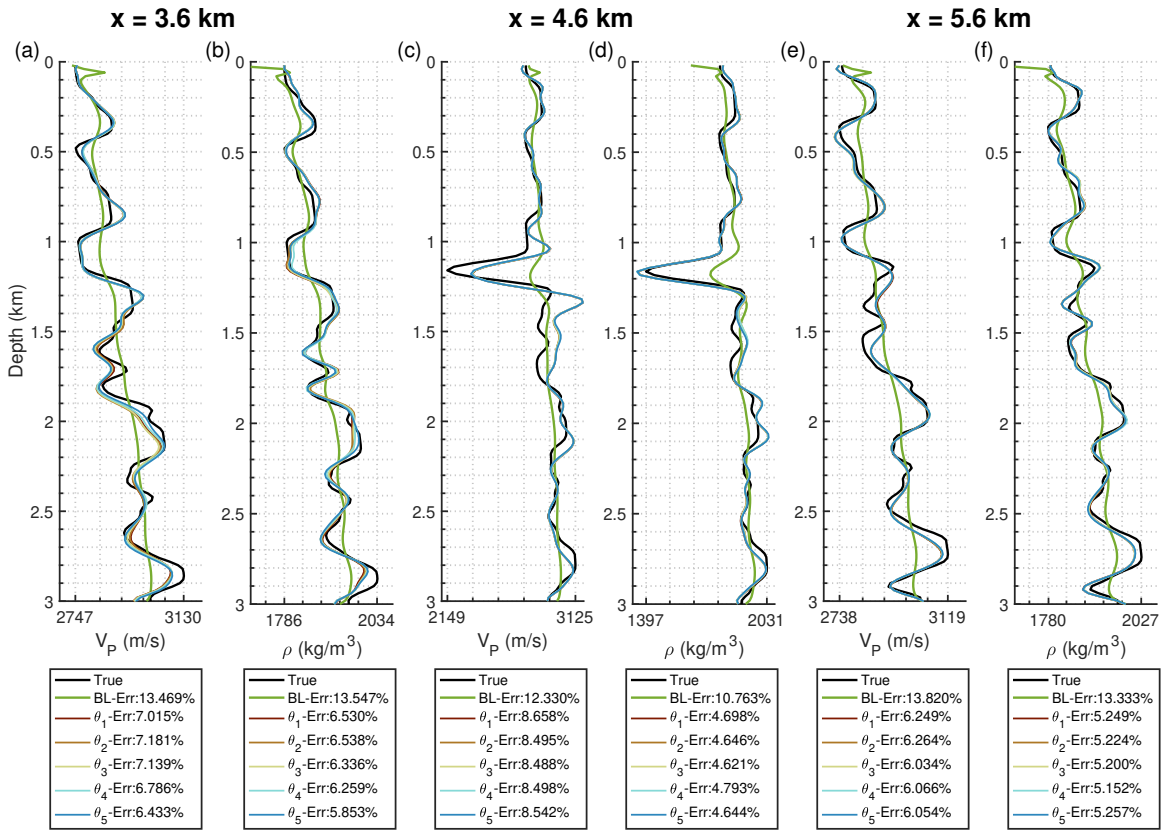

FIG. 13. Profiles in trajectory inclination test. (a), (c), and (e) are P-wave velocity cross-sections, while (b), (d), and (f) are density cross-sections.

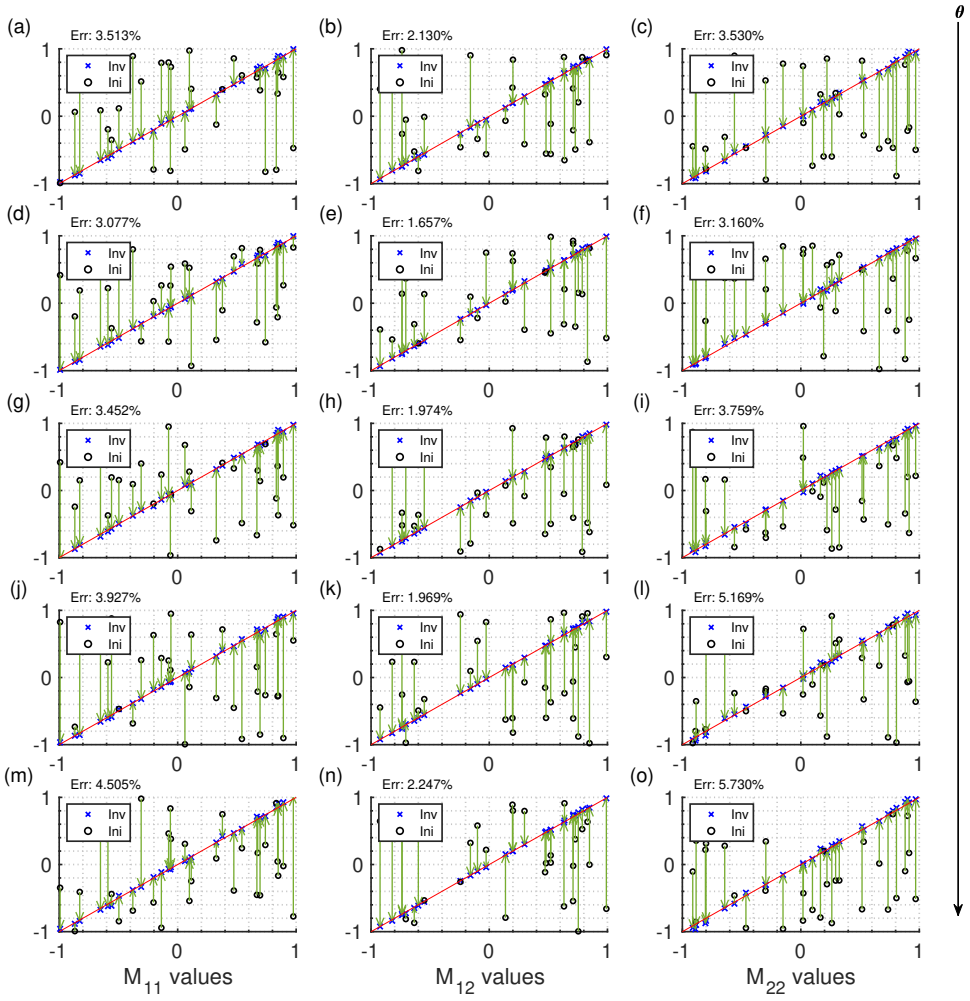

FIG. 14. Inversion of moment tensors. The black arrow denotes the gradual increment of θ, and the green arrows are from initial values to estimated values. (a)-(c) $\theta = 0°$. (d)-(f) $\theta = 22.5°$. (g)-(i) $\theta = 45°$. (j)-(l) $\theta = 67.5°$. (m)-(o) $\theta = 90°$.

Trajectory extension test

The experiments in this section aim at the possible effect of the change of drilling path extension. Figure (15) shows the schematic acquisition used in this test. We keep the inclination to be $45°$ and N_S to be 30 while going through five cases with different trajectory lengths. The extension L in the first case is 450 meters with clustering sources, while the drilling length is 1500 meters with a relatively sparse source distribution.

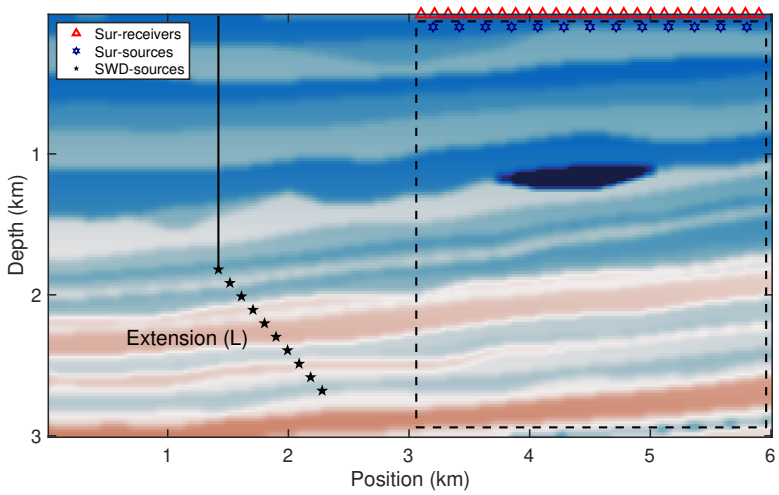

FIG. 15. Schematic acquisition system in trajectory extension test.

From the overall view in Figure (16), we can see a downgoing trend of the misfit in the V_P, but this trend does not apply to the ρ estimation. The profile that goes through the shallower low abnormaly shows the best result when we use the largest extension, as the illumination gets more comprehensive as it gets more comprehensive illumination when we enlarge the extension. However, it is hard to see a clear misfit tendency for the other profiles. The moment tensor inversions are stable as the cross plots present similar consistency between estimated and actual values. There seems to be little clear correlation between the misfits and drilling path length.

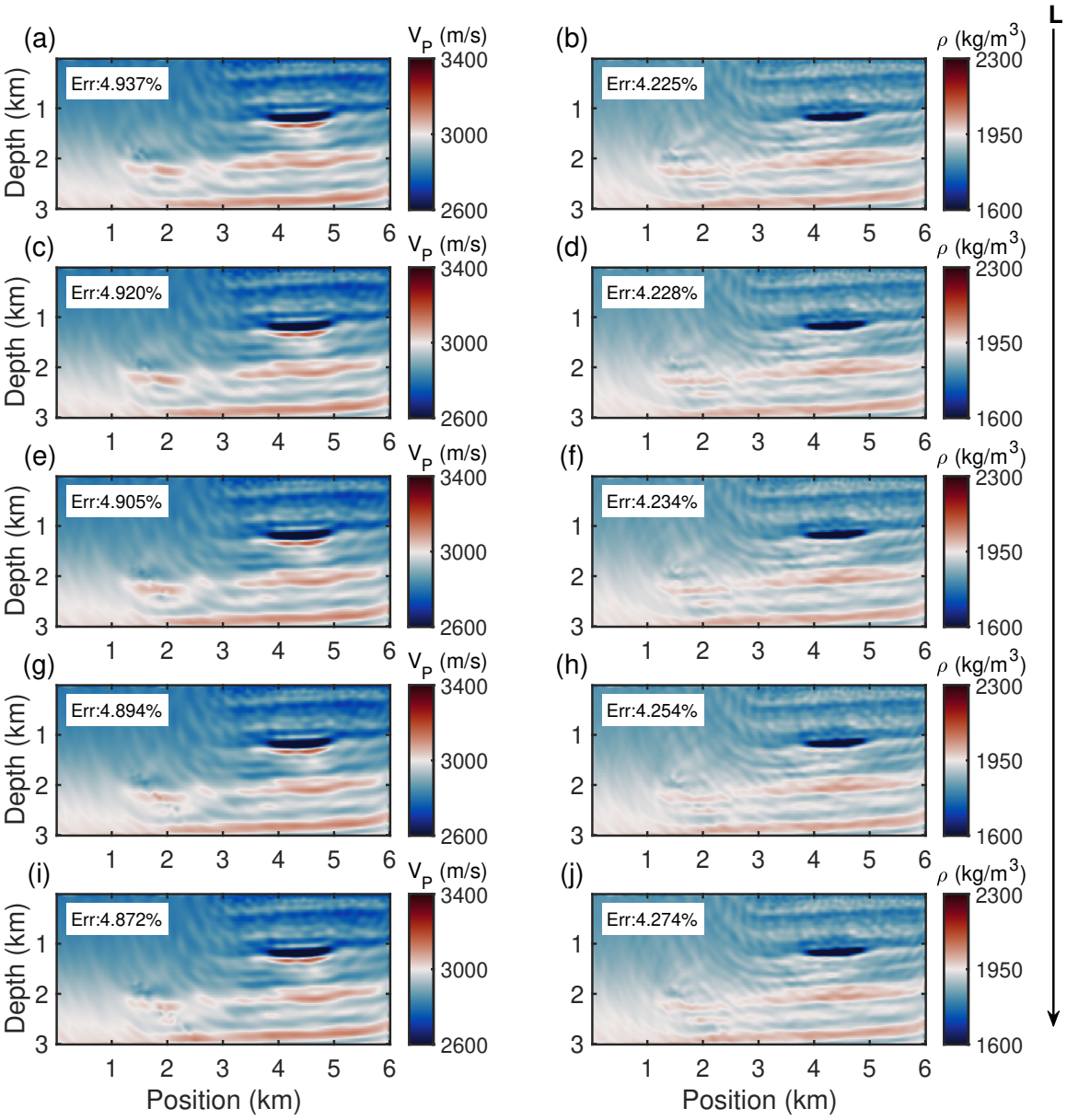

FIG. 16. Inversion of V_P and ρ with surface and SWD acquisitions with different trajectory extensions. The black arrow denotes the gradual increment of L. (a)-(b) inversion with $L = 450m$. (c)-(d) inversion with $L = 710m$. (e)-(f) inversion with $L = 975m$. (g)-(h) inversion with $L = 1250m$. (i)-(j) inversion with $L = 1500m$.

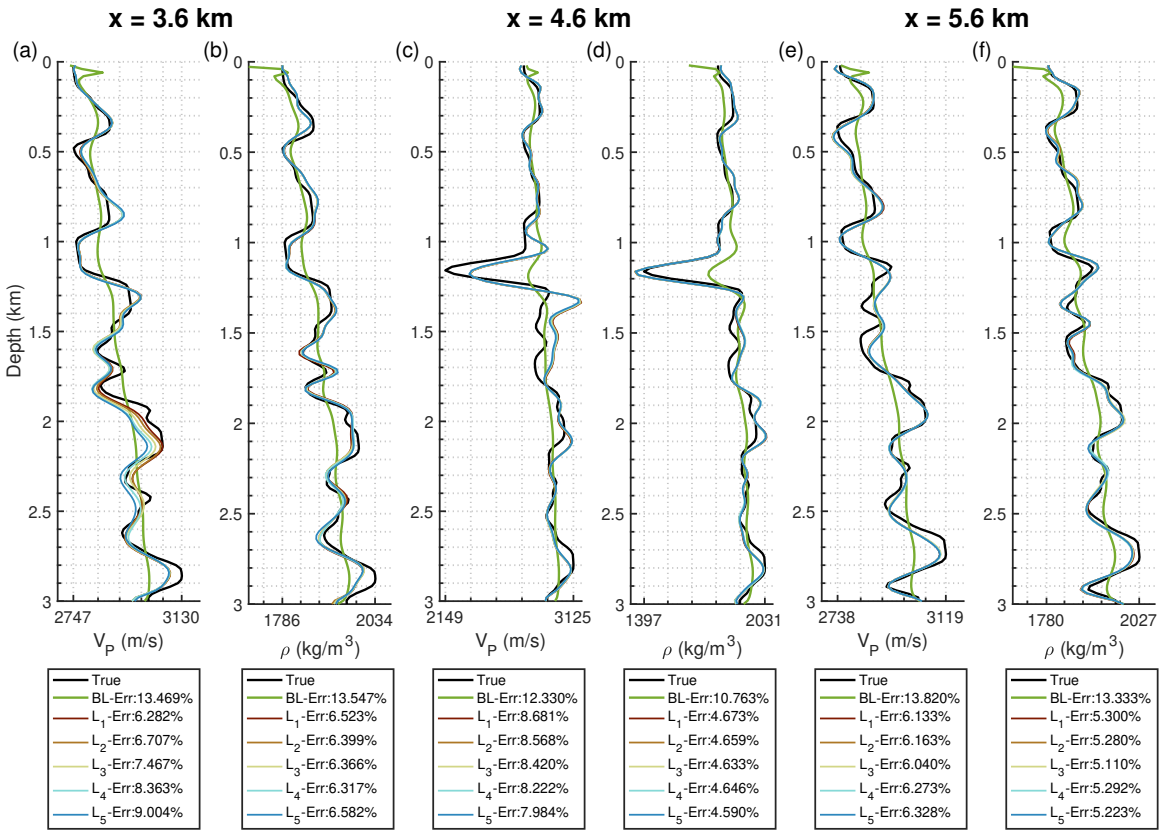

FIG. 17. Profiles in source number test. (a), (c), and (e) are P-wave velocity cross-sections, while (b), (d), and (f) are density cross-sections.

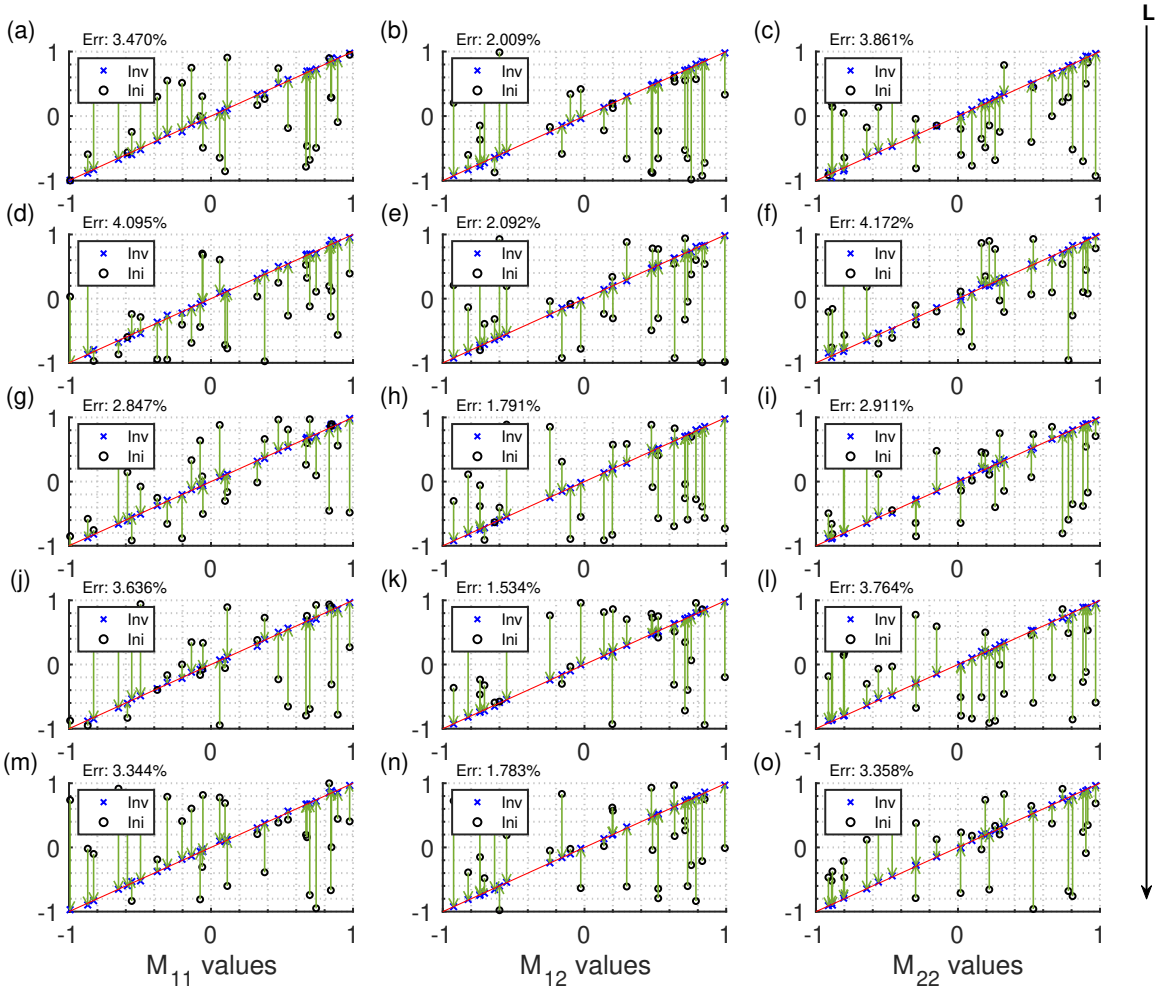

FIG. 18. Inversion of moment tensors. The black arrow denotes the gradual increment of L, and the green arrows are from initial values to estimated values. (a)-(c) $L = 450m$. (d)-(f) $L = 710m$. (g)-(i) $L = 975m$. (j)-(l) $L = 1250m$. (m)-(o) $L = 1500m$.

Simultaneous inversion for subsurface parameters, moment tensors and source positions

Some drilling programs usually have deviations between the designated and the actual wellbores because of the dip angle, hardness, and other formation or designing properties. This section considers recovering P-wave velocity, density, source radiations, and positions with the above simultaneous inversion scheme in a more realistic situation. The estimated discrete source positions will be connected to depict the estimated drilling path.

The same synthetic models are kept in this experiment. We use a larger offset from the drilling site to surface sensors for the geometry to eliminate the potential mistakes from misupdated source positions. The initial well trajectory is shown by the purple line, while the true path deviates from it as the yellow line in Figure (19). This test assumes that the SWD sources are radiating independently from their positions.

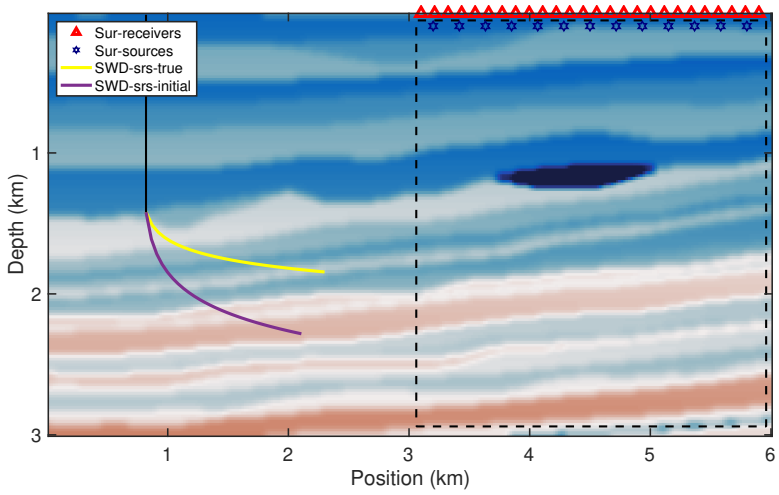

FIG. 19. Schematic acquisition system considering source positions.

The FWI for P-velocity and density models are also significantly enhanced with the intervention of SWD sources, suggesting the robustness of the FWI is kept despite the more nonlinear inverse problem with the involvement of unknown positions. However, the larger RMSPE values indicate the models are less effectively updated as all the inversions where only the radiation exists as source unknowns. This is also reflected by small deviations in cross plots of moment tensors. However, as shown by Figure (22), the discrete source positions depict an accurate inversion of the drilling trajectory.

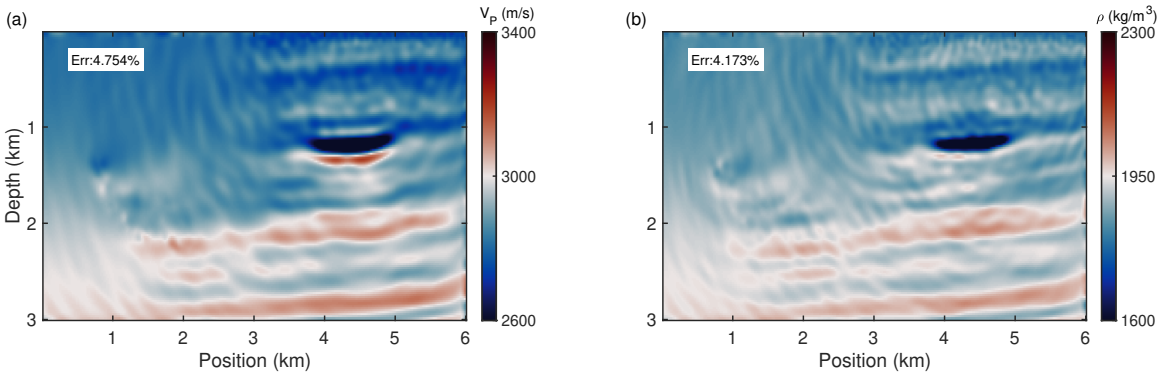

FIG. 20. Inversion of V_P and ρ with surface and SWD acquisitions with SWD radiation and position unknowns. (a) V_P model. (b) ρ model.

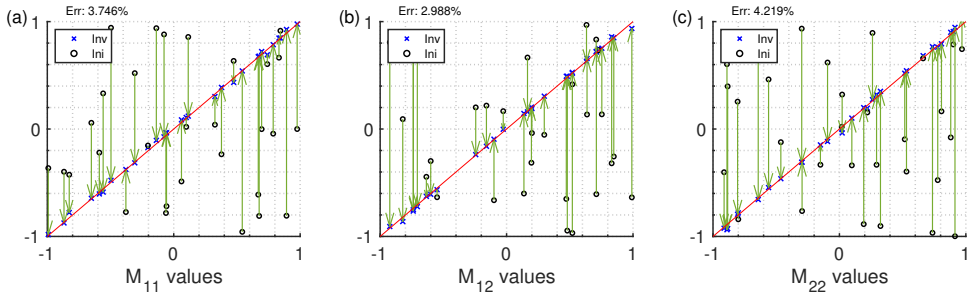

FIG. 21. Inversion of moment tensors when positions join as source unknowns. (a) M_{11} results. (b) M_{12} results. (c) M_{22} results.

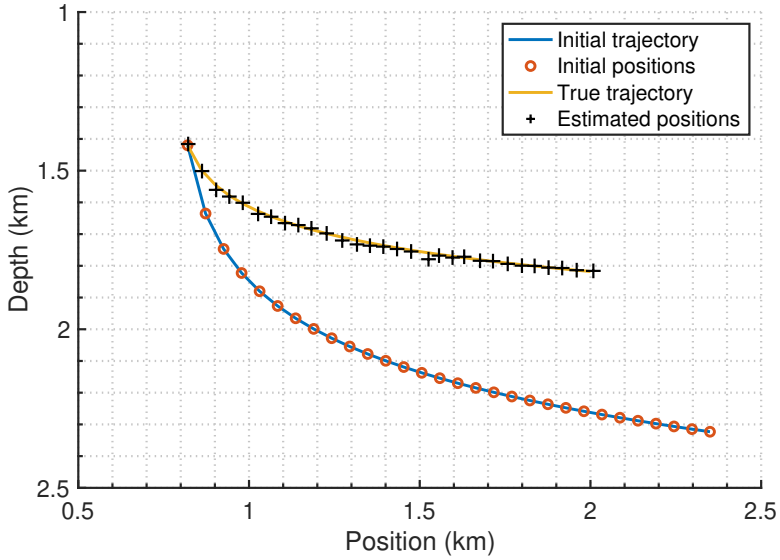

FIG. 22. Inversion for SWD source positions. The blue line denotes the initial trajectory, the yellow line shows the true trajectory, and the red and black markers are the discrete initial and estimated source positions, respectively.

Inversion with frequency variations

Our multi-band inversion currently uses random moment tensors with constant impulsive energy in each frequency, and the treatment of frequencies is quite simplified and ideal. The experiments in this section are designated to test the FWI performance in several scenarios where lower frequencies are missing. We use the most consistent acquisition in which there is a deviated trajectory with fixed inclination, extension, and source numbers (case 3 in the extension and inclination test, last case in the source number test). The varying parameter is the frequency spectrum. Figure (23) shows four frequency settings, where F_1 - F_4 denote weaker energy of the low frequencies. We conduct the simultaneous inversion for P-wave velocity, density, and moment tensor values while excluding source positions in the inversion variables to simplify this problem.

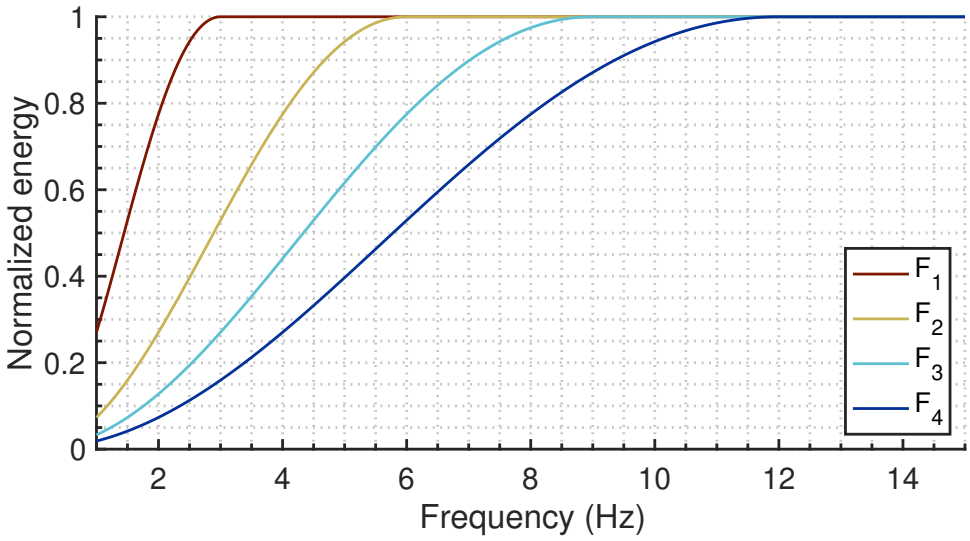

FIG. 23. Frequency components in this section's tests.

Poorer recovered models are acquired when the inversion is conducted with relatively higher frequencies, but the shallow low abnormaly is still characterized because of the increased illumination. Compared with the baseline inversion, where there is a feasible spectrum, the contribution from the SWD-generated datasets is self-evident. The results are gradually refined when more low-frequency components are included, although major errors cluster around unknown sources. The radiation inversions show a similar correlation with the intervention of lower frequency components. This section suggests that, in practical applications, the SWD is also supportive even with a lack of low frequencies.

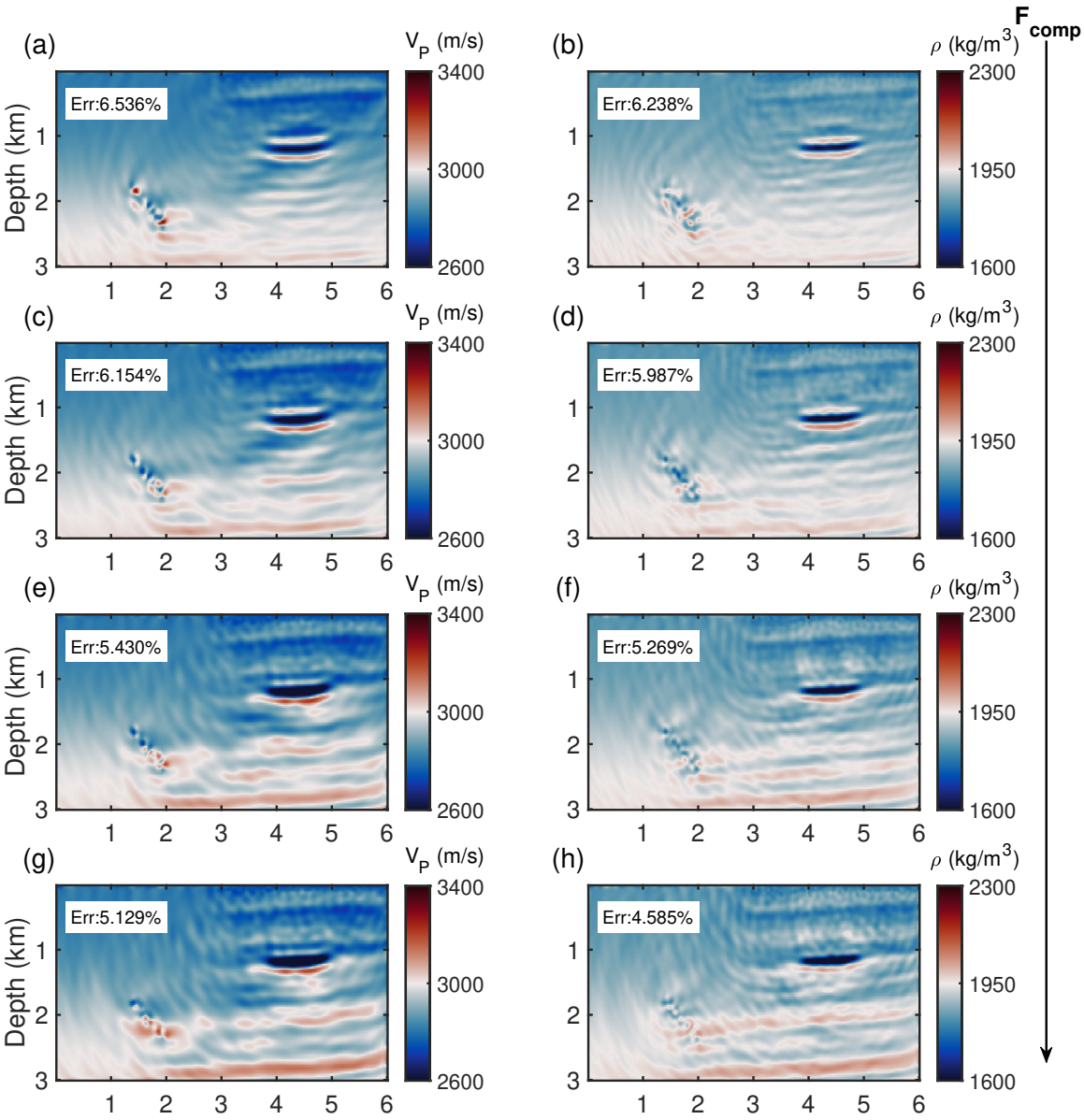

FIG. 24. Inversion of V_P and ρ with surface and SWD acquisitions with different frequency spectrums. The black arrow denotes spectrums with more comprehensive frequencies. (a)-(b) inversion with F_4. (c)-(d) inversion with F_3. (e)-(f) inversion with F_2. (g)-(h) inversion with F_1.

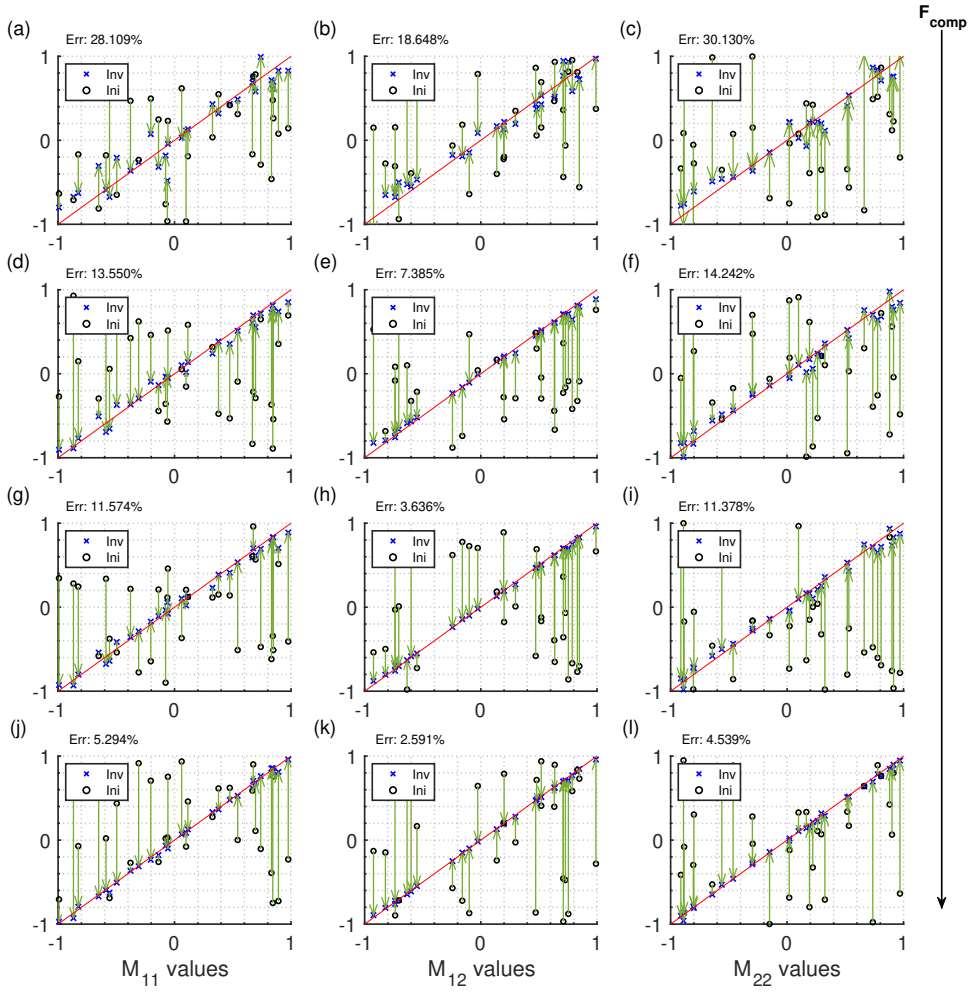

FIG. 25. Inversion of moment tensors. The black arrow denotes the gradual increment of θ, and the green arrows are from initial values to estimated values. (a)-(c) $\theta = 0°$. (d)-(f) $\theta = 22.5°$. (g)-(i) $\theta = 45°$. (j)-(l) $\theta = 67.5°$.

DISCUSSION

The synthetic examples show that a source-model simultaneous inversion is feasible in a surface + SWD setting. The simulations allow the impact of the additional ray paths to be understood and analyzed by comparing the FWI results with surface-only and surface-well acquisitions. In this SWD-FWI setting, we mitigate the nonlinearity by assuming known isotropic source radiation in the conventional acquisition, which helps in the inversion of V_P and ρ because the source-prior nature of our algorithm will downgrade the subsurface models' updating within the limited iterations we use. Better reconstructed V_P and ρ models can be obtained with explosive surface sources with generally radiating SWD sources along a plausible well trajectory. The enhancement varies by applying different acquisition situations, which shows a directional preference caused by the arrangement of surface geophones. The drilling path can also be depicted with the estimation of discrete sources via this simultaneous model + source inversion algorithm, which suggests the potential in managing the drilling programs.

We believe in this formulation that the critical elements needed to explain the SWD signature and begin to use it are in place. This study also suggests some important directions for further research. First, although we have not allowed it to be a free unknown yet, this framework can estimate source-related unknowns, thus enabling SWD-FWI technology to help refine drill position estimates. Moment tensor decomposition can also be applied to analyze the mechanisms of the bit-rock interaction if force couples can describe the discrete SWD sources. Such inversion has the potential to help the ahead-of-the-bit estimation in SWD, though computational speed and expense would need to be reduced for this to be practically realized. Another challenge is the source frequency spectrum in this problem. The dominant frequencies of SWD sources with the bit penetration could be higher than the typical frequency band in FWI, and there are some related issues, as discussed in one experiment section, to be considered in this simultaneous inversion approach since it is currently conducted with lower frequencies. However, it is possible to design a more realistic representation considering both the drill-bit-rock mechanism with moment tensors and frequency dependence.

CONCLUSIONS

This work explores the potential of taking advantage of the seismic-while-drilling data to compensate for the incomplete surface acquisition in simultaneous full-waveform inversion. Numerical examples demonstrate that the additional ray paths provided in an SWD dataset help to provide a better FWI result. The inclusion of SWD data improves the inversion of elastic properties, and this leads us to conclude that seismic-while-drilling data offers the potential to enhance inversion results. Besides, the radiation and position unknowns of the underground sources can also be precisely depicted, which shows a promising possibility that the drilling application can be monitored while implementing its datasets to the FWI. Further research is still required to provide more comprehensive conclusions, especially concerning a more precise moment tensor representation of the drill-bit rock interaction mechanisms and an advanced inversion strategy that will fit a more practical case. Additionally, the source signature of various types of drill bits should be quantified to detail the P and S-wave components.

ACKNOWLEDGEMENTS

We thank the sponsors of CREWES for their continued support. This work was funded by CREWES industrial sponsors and NSERC (Natural Science and Engineering Research Council of Canada) through the grant CRDPJ 543578-19.

REFERENCES

Aki, K., and Richards, P., 2002, Quantitative Seismology, Geology Seismology: University Science Books.

Aragao, O., and Sava, P., 2020, Elastic full-waveform inversion with probabilistic petrophysical model constraints: GEOPHYSICS, **85**, No. 2, R101–R111.

Auriol, J., Kazemi, N., and Niculescu, S.-I., 2021, Sensing and computational frameworks for improving drill-string dynamics estimation: Mechanical Systems and Signal Processing, **160**, 107,836.

Bertelli, L., and di Cesare, F., 1999, Improving the subsurface geological model while drilling: First Break, **17**, No. 6.

Brittan, J., Bai, J., Delome, H., Wang, C., and Yingst, D., 2013, Full waveform inversion - the state of the art: First Break, **31**, 75–81.

Brittan, J., and Jones, I., 2019, Fwi evolution — from a monolith to a toolkit: The Leading Edge, **38**, No. 3, 179–184.

Brossier, R., Etienne, V., Operto, S., and Virieux, J., 2010, Frequency-Domain Numerical Modelling of Visco-Acoustic Waves Based on Finite-Difference and Finite-Element Discontinuous Galerkin Methods.

Brossier, R., Operto, S., and Virieux, J., 2009, Seismic imaging of complex structures by 2d elastic frequency-domain full-waveform inversion: Geophysics, **74**.

Cheadle, S. P., Brown, R. J., and Lawton, D. C., 1991, Orthorhombic anisotropy: A physical seismic modeling study: GEOPHYSICS, **56**, No. 10, 1603–1613.

Eaid, M., Keating, S., and Innanen, K. A. H., 2022, Combined elastic fwi of accelerometer and das vsp data from a co2 sequestration test site in newell county, alberta.

Fichtner, A., 2011, Full Seismic Waveform Modelling and Inversion:

Fichtner, A., Kennett, B. L. N., Igel, H., and Bunge, H.-P., 2008, Theoretical background for continental- and global-scale full-waveform inversion in the timeâ€“frequency domain: Geophysical Journal International, **175**, No. 2, 665–685.

Jannane, M., Beydoun, W., Crase, E., Cao, D., Koren, Z., Landa, E., Mendes, M., Pica, A., Noble, M., Roeth, G., Singh, S., Snieder, R., Tarantola, A., Trezeguet, D., and Xie, M., 1989, Wavelengths of earth structures that can be resolved from seismic reflection data: GEOPHYSICS, **54**, No. 7, 906–910.

Kazemi, N., Auriol, J., Innanen, K. A. H., Shor, R., and Gates, I., 2021, Successive full-waveform inversion of surface seismic and seismic-while-drilling datasets without low frequencies, **2021**, No. 1, 1–5.

Kazemi, N., and Sacchi, M. D., 2014, Sparse multichannel blind deconvolution: GEOPHYSICS, **79**, No. 5, V143–V152.

Kazemi, N., Shor, R., and Innanen, K. A. H., 2018, Illumination compensation with seismic-while-drilling plus surface seismic imaging, **2018**, No. 1, 1–5.

Kazemi, N., Wong, J., Zhang, H., Bertram, K., Innanen, K., and Shor, R., 2020, Seismic illumination analysis through physical modeling.

Keating, S., and Innanen, K. A. H., 2020, Simultaneous recovery of source locations, moment tensors and subsurface models in 2D FWI, CREWES Research Report, 32, 33, 14.

Kerrison, H., Fallon, P., Kaszycka, E., Cichy, K., Ratcliffe, A., and Masmoudi, N., 2021, Impact of streamer acquisition geometry on fwi imaging, **2021**, No. 1, 1–5.

Khaled, O. S., Al-Ateeqi, A. M., James, A. R., and Meehan, R. J., 1996, Seismic-While-Drilling in Kuwait Results and Applications: GeoArabia, **1**, No. 4, 531–550.

Liu, Y., He, B., Zhang, Z., Zheng, Y., and Li, P., 2020, Reflection intensity waveform inversion: GEOPHYSICS, **85**, 1–72.

Martinez, A., Useche, M., and Guerra, R., 2020, Use of fiber optic acoustics to improve drilling efficiency and well placement, *in* OTC Offshore Technology Conference, vol. Day 1 Mon, May 04, 2020.

Métivier, L., Brossier, R., Operto, S., and Virieux, J., 2015, Acoustic multi-parameter FWI for the reconstruction of P-wave velocity, density and attenuation: preconditioned truncated Newton approach, 1198–1203.

Métivier, L., Brossier, R., Operto, S., and Virieux, J., 2017, Full waveform inversion and the truncated newton method: SIAM Review, **59**, No. 1, 153–195.

Métivier, L., Brossier, R., Virieux, J., and Operto, S., 2013, Full waveform inversion and the truncated newton method: SIAM Journal on Scientific Computing, **35**, No. 2, B401–B437.

Miranda, F., Aleotti, L., Abramo, F., Poletto, F., Craglietto, A., Persoglia, S., and Rocca, F., 1996, Impact of the seismic while drilling technique on exploration wells: First Break, **14**, No. 2.

Mothi, S., Schwarz, K., and Zhu, H., 2014, Impact of full-azimuth and long-offset acquisition on Full Waveform Inversion in deep water Gulf of Mexico, 317–321.

Nash, S. G., 2000, A survey of truncated-newton methods: Journal of Computational and Applied Mathematics, **124**, No. 1, 45–59, numerical Analysis 2000. Vol. IV: Optimization and Nonlinear Equations.

Naville, C., Serbutoviez, S., Throo, A., Vincké, O., and Cecconi, F., 2004, Seismic while drilling (swd) techniques with downhole measurements, introduced by ifp and its partners in 1990-2000: Oil & Gas Science and Technology-revue De L Institut Francais Du Petrole, **59**, 371–403.

Nocedal, J., and Wright, S., 2006, Numerical Optimization, Springer Series in Operations Research and Financial Engineering: Springer New York.

Pan, W., Innanen, K., and Geng, Y., 2018, Elastic full-waveform inversion and parametrization analysis applied to walk-away vertical seismic profile data for unconventional (heavy oil) reservoir characterization: Geophysical Journal International, **213**, 1934–1968.

Pan, W., Innanen, K. A., Geng, Y., and Li, J., 2019, Interparameter trade-off quantification for isotropic-elastic full-waveform inversion with various model parameterizations: GEOPHYSICS, **84**, No. 2, R185–R206.

Plessix, R.-E., 2006, A review of the adjoint-state method for computing the gradient of a functional with geophysical applications: Geophysical Journal International, **167**, No. 2, 495–503.

Podgornova, O., Leaney, S., and Liang, L., 2018, Resolution of vti anisotropy with elastic full-waveform inversion: Theory and basic numerical examples: Geophysical Journal International, **214**, 200–218.

Poletto, F., Corubolo, P., Farina, B., Schleifer, A., Pollard, J., Peronio, M., and Böhm, G., 2012, Drill-bit SWD and seismic interferometry for imaging around geothermal wells, 4319–4324.

Poletto, F., and Miranda, F., 2004, Seismic While Drilling: Fundamentals of Drill-Bit Seismic for Exploration, Handbook of Geophysical Exploration: Seismic Exploration: Elsevier Science.

Poletto, F., Petronio, L., Miranda, F., Malusa, M., Schleifer, A., Corubolo, P., Bellezza, C., Miandro, R., and Gressetvold, B., 2003, Prediction and 3d imaging while drilling by drill-bit 3d rvsp.

Pratt, R., 1999, Seismic waveform inversion in the frequency domain, part 1: Theory and verification in a physical scale model: Geophysics, **64**, 888–901.

Pratt, R., Shin, C., and Hicks, 1998, Gauss-newton and full newton methods in frequency-space seismic waveform inversion: Geophysical Journal International, **133**, 341 – 362.

Pratt, R., and Shipp, R., 1999, Seismic waveform inversion in the frequency domain, part 2: Fault delineation in sediments using crosshole data: Geophysics, **64**, 902–914.

Pratt, R. G., 1990, Frequency-domain elastic wave modeling by finite differences: A tool for crosshole seismic imaging: GEOPHYSICS, **55**, No. 5, 626–632.

Pratt, R. G., Song, Z.-M., Williamson, P., and Warner, M., 1996, Two-dimensional velocity models from wide-angle seismic data by wavefield inversion: Geophysical Journal International, **124**, No. 2, 323–340.

Rector, J. W., and Hardage, B. A., 1992, Radiation pattern and seismic waves generated by a working roller-cone drill bit: Geophysics, **57**, No. 10, 1319–1333.

Rocca, F., Vassallo, M., and Bernasconi, G., 2005, Three-dimensional seismic-while-drilling (swd) migration in the angular frequency domain: GEOPHYSICS, **70**, No. 6, S111–S120.

Sheppard, M., and Lesage, M., 1988, The Forces at the Teeth of a Drilling Rollercone Bit: Theory and Experiment.

Shin, C., Jang, S., and Min, D.-J., 2008, Improved amplitude preservation for prestack depth migration by inverse: Geophysical Prospecting, **49**, 592 – 606.

Singh, S., Tsvankin, I., and Z. Naeini, E., 2018, Bayesian framework for elastic full-waveform inversion with facies information: The Leading Edge, **37**, 924–931.

Tape, W., and Tape, C., 2013, The classical model for moment tensors: Geophysical Journal International, **195**, 1701–1720.

Tarantola, A., 1984, Inversion of seismic reflection data in the acoustic approximation: GEOPHYSICS, **49**, No. 8, 1259–1266.

Tarantola, A., 2004, Inverse Problem Theory and Methods for Model Parameter Estimation: Society for Industrial and Applied Mathematics, USA.

Tiwari, D., Mao, J., and Ma, X., 2018, Refraction and reflection FWI for high-resolution velocity modeling in Mississippi Canyon, 1288–1292.

Vasconcelos, I., and Snieder, R., 2008, Interferometry by deconvolution: Part 2 — theory for elastic waves and application to drill-bit seismic imaging: Geophysics, **73**.

Vavrycuk, V., 2005, Focal mechanisms in anisotropic media: Geophysical Journal International, **161**, 334 – 346.

Vigh, D., Cheng, X., Jiao, K., Kang, W., and Brand, N., 2021, The impact of acquisition geometry on full-waveform inversion updates: The Leading Edge, **40**, No. 5, 335–341.

Virieux, J., and Operto, S., 2009, An overview of full-waveform inversion in exploration geophysics: GEOPHYSICS, **74**, No. 6, WCC1–WCC26.

Xing, G., and Zhu, T., 2020, Hessian-based multiparameter fractional viscoacoustic full-waveform inversion, 895–899.